Energy &
Environmental
Science

PAPER

View Article Online
View Journal | View Issue

Cite this: *Energy Environ. Sci.*, 2016, **9**, 2433

Water oxidation catalysis – role of redox and structural dynamics in biological photosynthesis and inorganic manganese oxides†

I. Zaharieva,*[a] D. González-Flores,[a] B. Asfari,[a] C. Pasquini,[a] M. R. Mohammadi,[a] K. Klingan,[a] I. Zizak,[b] S. Loos,[a] P. Chernev[a] and H. Dau*[a]

Received 26th April 2016,
Accepted 9th June 2016

DOI: 10.1039/c6ee01222a

www.rsc.org/ees

Water oxidation is pivotal in biological photosynthesis, where it is catalyzed by a protein-bound metal complex with a Mn_4Ca-oxide core; related synthetic catalysts may become key components in non-fossil fuel technologies. Going beyond characterization of the catalyst resting state, we compare redox and structural dynamics of three representative birnessite-type Mn(Ca) oxides (catalytically active *versus* inactive; with/without calcium) and the biological catalyst. In the synthetic oxides, Mn oxidation was induced by increasingly positive electrode potentials and monitored by electrochemical freeze-quench and novel time-resolved *in situ* experiments involving detection of X-ray absorption and UV-vis transients, complemented by electrochemical impedance spectroscopy. A minority fraction of Mn(III) ions present at catalytic potentials is found to be functionally crucial; calcium ions are inessential but tune redox properties. Redox-state changes of the water-oxidizing Mn oxide are similarly fast as observed in the biological catalyst (<10 ms), but 10–100 times slower in the catalytically inactive oxide. Surprisingly similar redox dynamics of biological catalyst and water-oxidizing Mn(Ca) oxides suggest that in both catalysts, rather than direct oxidation of bound water species, oxidation equivalents are accumulated before onset of the multi-electron O–O bond formation chemistry in Mn(III)–Mn(IV) oxidation steps coupled to changes in the oxo-bridging between metal ions. Aside from the ability of the bulk oxide to undergo Mn oxidation-state changes, we identify two further, likely interrelated prerequisites for catalytic activity of the synthetic oxides: (i) the presence of Mn(III) ions at catalytic potentials preventing formation of an inert all-Mn(IV) oxide and (ii) fast rates of redox-state changes approaching the millisecond time domain.

Broader context

In plants, algae and cyanobacteria, solar energy drives the splitting (oxidation) of water molecules resulting in O_2, protons and energized electrons (reducing equivalents). The latter are required for CO_2 reduction and formation of carbohydrates that fuel life on Earth. Catalysis of water oxidation is crucial not only in biological photosynthesis, but also in technology for production of non-fossil fuels. The present study links the biological catalysts to three exemplary synthetic manganese oxides resembling minerals. Similar redox-state and structural dynamics suggest a common basic mode of catalysis. Aside from the static atomic and electronic structures of the hydrated oxides, also type and rate of redox-state and associated structural changes could determine catalytic efficiency. Our results may support knowledge-guided development of future catalyst generations and enrich the discussion of biogenic oxides or metal ion sequestering (remediation).

Introduction

In biological photosynthesis, the water oxidation reaction is catalyzed by a Mn_4CaO_5 core cluster supplemented by four terminal water ligands and embedded in a protein complex denoted as photosystem II (PSII, Fig. 1a and b).[1–4] The five metal ions are closely connected by bridging oxygen atoms and bound to evolutionary highly conserved protein side chains (Fig. 1a).[5] The compact metal–oxo core of the catalyst resembles closely structural motifs of purely inorganic MnCa oxides.[6,7] The interrelation

---

[a] Freie Universität Berlin, Fachbereich Physik, Arnimallee 14, 14195 Berlin, Germany. E-mail: ivelina.zaharieva@fu-berlin.de, holger.dau@fu-berlin.de
[b] Helmholtz-Zentrum-Berlin, Institute for Nanometre Optics and Technology, Albert-Einstein-Straße 15, 12489 Berlin, Germany

† Electronic supplementary information (ESI) available: Materials and methods; scheme on freeze-quench XAS; cyclic voltammograms; XAS and UV-vis spectra; EXAFS simulation parameters; current and OCP transients; time-resolved experiment; and electrochemical impedance spectroscopy (EIS) data. See DOI: 10.1039/c6ee01222a

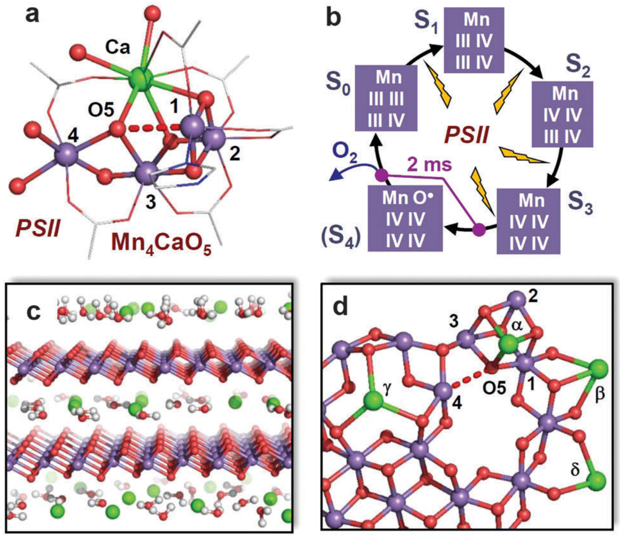

Fig. 1 Water oxidation in biology (top) and catalyzed by Mn(Ca) oxides (bottom). (a) Structural model of Mn_4CaO_5 cluster in PSII in its dark-stable S_1-state.[5] The Mn_4CaO_5 oxide core is bound to one imidazole and six carboxylate sidechains of the PSII proteins (Mn atoms are shown in magenta, Ca in green, O in red, C in gray, N in blue). The four terminal O-ligands are water species (Mn–OH_2 or Mn–OH); they are part of a protein-internal water cluster (which is not shown). The standard numbering of the four manganese ions (Mn1 to Mn4) and of one specific bridging oxygen (O5) is indicated. In the S_2-state, there is a dynamic transition between two redox isomers ($Mn1^{III}Mn4^{IV}$ *versus* $Mn1^{IV}Mn4^{III}$) differing in the position of O5 which is either bound to $Mn1^{IV}$ or to $Mn4^{IV}$.[21] (b) S-State cycle model of biological water oxidation. A sequence of saturating laser flashes of visible light can drive the protein-bound Mn_4Ca–oxo complex synchronously through its S-state cycle. Each laser flash induces oxidation of the Mn_4Ca complex and thus the corresponding $S_i \rightarrow S_{i+1}$ transition, where the subscript indicates the number of oxidizing equivalents accumulated by the Mn_4Ca complex.[22] (c) Structure of an idealized birnessite (based on coordinates of ref. 23; protons had been not resolved and were added to the interlayer water molecules for illustration only). (d) Illustrative scheme on the structural motifs in the electrodeposited water-oxidizing Mn(Ca) oxides based on X-ray absorption data.[13] In this panel, the green color marks manganese or calcium ions that are not part of the extended MnO_2 layers of well-ordered birnessites. They may bind on top of the MnO_2 layer resulting in a (distorted) $Mn_3(Mn/Ca)O_4$ cubane (α), or on top of a Mn vacancy of the hexagonal MnO_2 lattice (γ), or at the margin of MnO_2 fragments of limited size (β and δ). Not all oxygen ligands but only the oxygen atoms bridging between the depicted metal ions are shown.

between the worlds of biochemistry and inorganic oxides[7–10] is of interest regarding both the evolution of oxygenic photosynthesis and the development of synthetic water-oxidation catalysts.

Manganese oxides exist as many different polymorphs.[6] The ones with sizeable catalytic activity towards water oxidation are often non-crystalline materials without well-resolved Bragg reflections when studied by X-ray powder diffraction.[11] Their structure has been identified by X-ray absorption spectroscopy (XAS) as highly disordered birnessite-like oxide layers (oxide sheets) consisting mostly of edge-sharing MnO_6 octahedra, a structural motif which also can be viewed as Mn pairs connected by di-μ-oxo bridges (Fig. 1c and d).[11–15] Crystalline manganese oxides have also been reported as being catalytically active.[16–19] Under the strongly oxidizing conditions required for water oxidation, amorphisation of the crystalline oxide material is likely.[18,20] The amorphisation starts at the surface and may be paralleled by a continuous increase of the catalytic activity in the bulk volume of the material.

In the present work, to avoid the ambiguities of active-site formation by surface amorphization, we investigate fully amorphous, hydrated oxides. They can be viewed as layer fragments of oxo-hydroxides interfaced by a quasi-electrolyte consisting of water molecules and typically also cations (*e.g.* potassium) and anions (*e.g.* phosphate, carbonate). This quasi-electrolyte can provide the substrate water molecules of the water-oxidation reaction and facilitates proton transport. Consequently, water oxidation catalysis is not limited to the outer surface of the catalyst film, but takes place throughout the bulk volume of the catalyst film, presumably at the margins or defect sites of the oxide fragments.[24–28] We note that the hydrated oxides as they are described above are most likely equivalent to the 'hydrous oxides' reviewed in ref. 29. The volume activity of these hydrated (or hydrous) oxides favors experimental tracking of redox dynamics and water oxidation catalysis strongly because bulk-sensitive spectroscopic methods can provide mechanistic insights.

Here we compare oxidation state and structural dynamics of the biological catalyst, the protein-bound Mn_4Ca–oxo cluster of PSII, and of three representative birnessite-type Mn(Ca) oxides. The three synthetic oxides are (i) a catalytically active, water-oxidizing Mn oxide,[13] (ii) a redox-active, but catalytically inactive Mn oxide,[13] and (iii) a catalytically active MnCa oxide.[30] Using electrochemical quasi-*in situ*, freeze-quench X-ray absorption spectroscopy complemented by time-resolved detection of XAS signals, UV-vis and impedance spectroscopy, we go beyond characterization of the resting state of the synthetic catalysts and approach comparison of their oxidation-state and structural dynamics. This approach facilitates atomistic insight in both, the biomimetic character of the functionality of the synthetic oxides and the crucial determinants of catalytic function of Mn(Ca) oxides.

Materials and methods

Reagents

$Mn(CH_3COO)_2\cdot 4H_2O$ (Fluka, ≥99%), H_2KPO_4 (Roth, ≥99%), K_2HPO_4 (Roth, ≥99%), $Ca(CH_3COO)_2\cdot 4H_2O$ (Fluka, 99%), H_3BO_3, (Merck, p.A.), KOH (Sigma Aldrich, ≥86%). All reagents where used without further purification. Solutions were prepared with 18 MΩ cm Milli-Q water.

Mn(Ca) film deposition

All catalysts films were deposited electrochemically on the anode using a standard three-electrode setup (potentiostat SP-300, BioLogic; Ag/AgCl reference electrode and Pt-mesh counter electrode). The electrode substrate was thin (100 μm) glassy carbon (HTW Hochtemperatur-Werkstoffe GmbH) with an electrolyte-exposed area of 10 × 14 mm for XAS measurements or an indium-doped tin oxide (ITO) covered glass electrodes (Visiontek Systems Ltd) with an electrolyte-exposed area of 1 cm^2 for impedance and UV-vis spectroscopy. The electrodeposition procedures are described previously and result in deposition of similar amount of Mn (about 5 μg cm^{-2} or 90 nmol cm^{-2}).[4,30] In brief, the catalytically active Mn oxide (MnCat) and the essentially inactive Mn oxide were deposited from aqueous solution of 0.5 mM $Mn^{II}(CH_3COO)_2$ by 25 cyclic voltammograms (CVs), for the MnCat (from 2.15 to −0.75 V *vs.* NHE, 100 mV s^{-1}) or at constant potential, for the inactive oxide (15 min at 1.35 V *vs.* NHE), as described previously.[13] The mixed MnCa oxide was deposited at constant potential (1.45 V *vs.* NHE) applied for 15 min in 0.1 M borate buffer (pH 9.2) containing 0.5 mM $Mn^{II}(CH_3COO)_2$ and 0.1 mM $Ca(CH_3COO)_2$ and subsequently annealed for 3 h at 210 °C in air.[30] Compensation for the ohmic resistance of electrolyte and electrode (*iR* compensation) was not employed.

Freeze-quench X-ray absorption experiment

Mn(Ca) oxides deposited on thin glassy carbon were frozen after 3 min exposure to the selected potential in 0.1 M phosphate buffer adjusted to pH 7, see also ref. 28 and ESI,† Fig. S1. XAS at the Mn K-edge was performed at the BESSY II synchrotron radiation source (Berlin-Adlershof) operated by the Helmholtz-Zentrum Berlin (beamlines KMC-1 and KMC-3) at 20 K (in Oxford He-flow cryostat). A silicon(111) double-crystal monochromator was used for scanning the X-ray excitation energy. All X-ray absorption spectra were collected in the fluorescence mode, using a 13-channel energy-resolving Ge detector (Canberra) with regions of interest adjusted at the Mn K_α fluorescence emission. In each scan, the X-rays that passed the catalyst sample were used to measure the absorption of $KMnO_4$ powder placed between two home-made ionization chambers. The $KMnO_4$ absorption was utilized for precise energy calibration; the maximum of the narrow pre-edge absorption peak of the $KMnO_4$ was set to 6543.3 eV. For further details on XAS data collection, data analysis and EXAFS simulations, see ref. 11 and 13 and ESI.†

Time-resolved *in situ* X-ray absorption measurements

The measurements were performed at 20 °C at the BESSY II synchrotron radiation source at beamline KMC-3. Manganese oxide deposited on thin glassy carbon was attached as a window to the wall of a home-made Teflon cell filled with 0.1 M phosphate buffer (adjusted to pH 7) and placed in the path of the X-ray beam. A silicon(111) double-crystal monochromator was used for selecting a fixed X-ray excitation energy (6553.3 eV). The fluorescence was monitored perpendicular to the incident beam by scintillation-photomultiplier detector assembly. For further details and an overview scheme of the time-resolved *in situ* experiment, see ESI,† Fig. S9.

Steady-state *in situ* UV-vis absorption measurements

UV-vis measurements were performed using a commercial UV-vis spectrophotometer (Cary 50, Varian). A quartz cuvette (2.5 cm × 2.5 cm × 4 cm height) filled with electrolyte (15 mL, 0.1 M phosphate buffer, pH 7) was placed in the optical compartment of the spectrometer. The semi-transparent working electrode (ITO-coated glass with electrodeposited Mn oxide film), a Hg/Hg_2SO_4 reference electrode and a platinum counter electrode were immersed in the electrolyte-filled cuvette. The electrochemistry was controlled by a potentiostat (Biologic SP-300).

Time-resolved *in situ* UV-vis experiment

Oxidation-state changes were tracked in the millisecond time domain by recording changes in the transmitted light (light emitting diode, Avago Technologies, peak wavelength 470 nm). A Mn oxide film electrodeposited on glass-supported ITO was operated in a quartz-glass electrochemical cell filled with 0.1 M phosphate buffer (pH 7) at room temperature. The film together with the cell was placed in the light path of the pulse-driven light-emitting diode (blue light; 50 kHz pulses, light-on and light-off periods of equal length). The transmitted light was detected by a silicon photodiode (1 cm^2) connected *via* a home-made current-to-voltage amplifier to a lock-in amplifier (Princeton Applied Research, model 5209). The lock-in output signal was recorded with time resolution of 10 ms by a potentiostat (Biologic SP-300), which also operated the electrochemical cell. For collection of the shown absorption, the working electrode was switched repeatedly between potential application (10 s at 1.4 V *vs.* NHE, pH 7) and open-circuit conditions (10 s); good reversibility was observed and 30 transients were averaged.

Electrochemical impedance spectroscopy (EIS)

EIS was performed with a Gamry Interface 1000™ potentiostat in 0.1 M phosphate buffer (pH 7, adjusted with 0.1 M KH_2PO_4 and 0.1 M K_2HPO_4). For each potential, a freshly prepared Mn oxide film was used. The reproducibility of the film preparation was confirmed by a sequence of 3 CVs from 0.9 to 1.45 V *vs.* NHE (ESI,† Fig. S2); the variability in the maximum catalytic current (measured at 1.45 V) did not exceed 10%. Before starting the EIS protocol (100 mHz to 10 kHz, 10 mV modulation amplitude of the working-electrode potential), the films were equilibrated at the respective potential for 2 min. The EIS data was simulated according to the equivalent circuit provided in ESI,† Fig. S12.

Results

Mn oxidation-state changes in biological and inorganic catalysts

Employing sequences of suitably spaced laser flashes of saturating intensity, the protein-bound Mn_4Ca complex of PSII can be driven synchronously through the so-called S-state cycle involving the intermediate states S_0 to S_4 (the subscript indicates the number of accumulated oxidizing equivalents, Fig. 1b[31]). The combination of flash sequences with a freeze-quench protocol has facilitated collection of X-ray absorption spectroscopy data for the S_0, S_1, S_2, and S_3 state; direct tracking of the oxidation state changes in room-temperature X-ray experiments confirmed the absence of freezing artefacts.[32] To facilitate comparisons with the synthetic Mn oxides, XAS spectra obtained previously for the biological catalyst[32,33] are shown in Fig. 2a and b.

In electrochemical water oxidation by Mn oxide films, oxidation state changes of the Mn ions in the amorphous catalyst film deposited on the anode can be induced by application of suitable

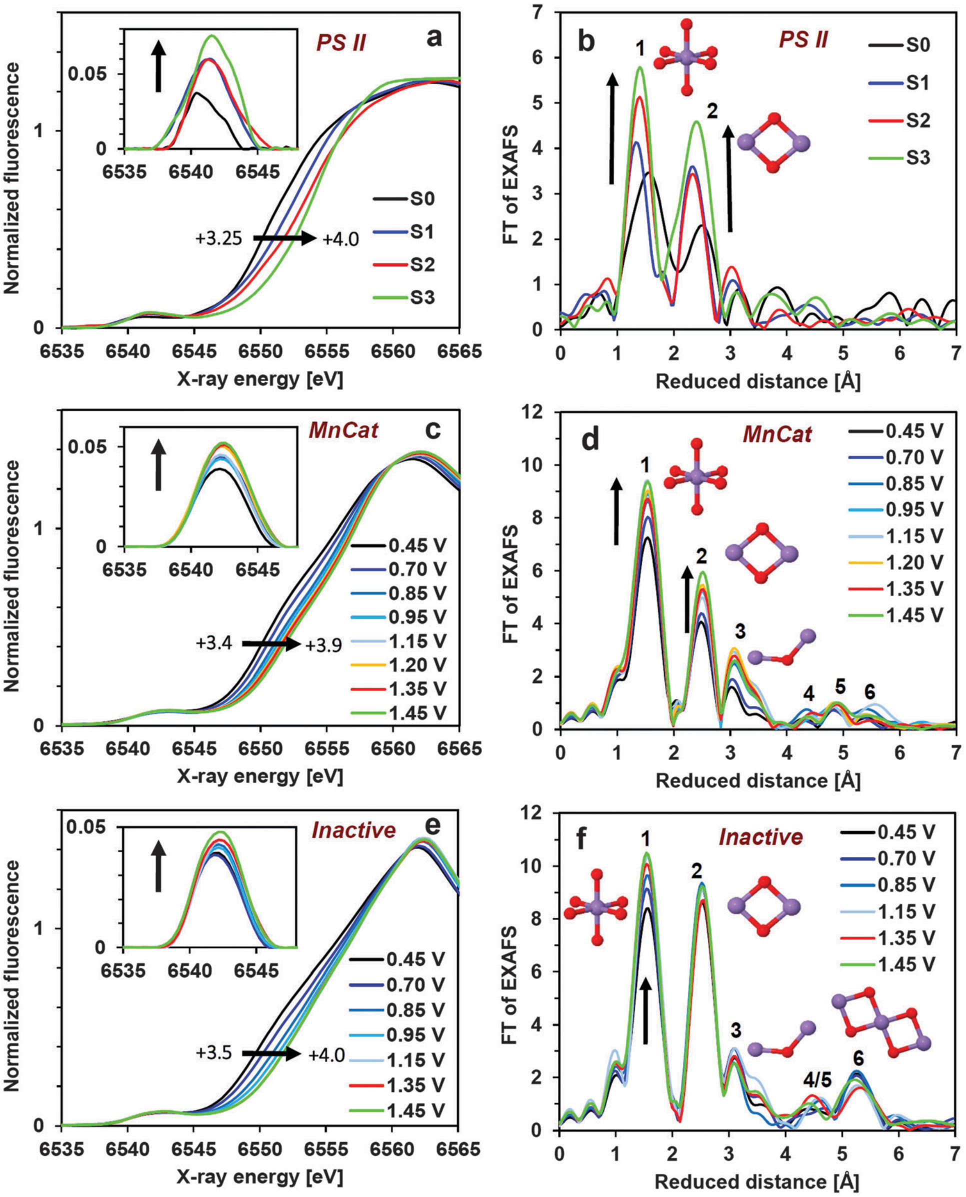

Fig. 2 XANES and EXAFS spectra of the protein-bound Mn_4Ca complex of PSII and of electrodeposited Mn oxides. (a) XANES and (b) EXAFS of the Mn_4Ca complex of PSII for the four semi-stable intermediates of the S-state cycle (Fig. 1b, data from ref. 32). (c) XANES and (d) EXAFS of electrodeposited Mn oxide with water-oxidation activity (MnCat), where oxidation state changes were induced by application of the indicated electrode potential for 3 min. (e) XANES and (f) EXAFS of catalytically inactive Mn oxide. See ESI,† Fig. S7, for XANES and EXAFS of the MnCa oxide. The insets in (a), (c) and (e) illustrate changes in the magnitude of the pre-edge feature extracted from the XANES data by background subtraction; we note that the spectral resolution had been lower in the (c) and (e) data than in (a) so that some pre-edge fine-structure is visible in (a) only. In the Fourier-transformed (FT) EXAFS spectra, the indicated 'reduced distance' is by about 0.4 Å shorter than the precise Mn–ligand distance as determined by EXAFS simulations (ESI,† Table S1). For each FT peak, the corresponding structural motif is schematically shown (Mn, magenta; O, red). The indicated electrode potentials are referenced *versus* NHE (0.1 M phosphate buffer, pH 7).

electrode potentials for short time periods (3 min in this study). This time period is sufficiently long to establish a stable redox equilibrium of the Mn ions within the oxide film, but short enough to avoid phase transitions of the oxide material as they have been observed previously.[34] Then the electrode assembly was rapidly frozen by immersion in liquid nitrogen, followed by storage at 77 K and XAS data acquisition at 20 K (ESI,† Fig. S1). This freeze-quench approach is superior to *in situ* experiments at room temperature with respect to data quality and significance (less damped oscillatory structure in the spectra at higher excitation energy) as well as avoidance of radiation damage.[28] It was used for collecting the XAS spectra of the three synthetic oxides, each equilibrated at 7–8 electrochemical potentials.

Fig. 2 compares changes in the XANES (X-ray absorption near-edge structure) of the Mn_4Ca complex bound to the PSII proteins with spectra of a catalytically active Mn oxide, which were synthesized by electrodeposition at alternating electrical potentials (MnCat).[13] In the S_0 state (lowest oxidation state) of the biological catalyst, three Mn^{III} ions and one Mn^{IV} result in an average Mn oxidation state of +3.25. Each laser flash drives the oxidation of one Mn^{III} ion until in the S_3, an all-Mn^{IV} state is reached.[35] These oxidation state changes are reflected by a shift of the X-ray absorption edge to higher energies.[36,37] When comparing the biological catalyst (Fig. 2a) and the synthetic, catalytically active Mn oxide (MnCat, Fig. 2c), we observe similar shifts of the X-ray edge position. Calibration with structurally characterized Mn oxides provides estimates of the average Mn oxidation state (n_{ox}; calibration line is shown in the ESI,† Fig. S3). In the MnCat, n_{ox} changes from +3.4 (at 0.45 V) to +3.9 (at 1.45 V) suggesting about 60% Mn^{III} at 0.45 V and 10% Mn^{III} at the most positive potentials. Similar results regarding the Mn oxidation states are obtained by bond-valence sum calculation (ESI,† Fig. S5) with Mn–O bond lengths obtained by EXAFS simulations.

Oxidation-coupled structural changes in biological and inorganic catalysts

Interestingly, not only energy and absolute magnitude of the pre-edge feature visible in the XANES spectra are highly similar in PSII[38] and the synthetic oxides, but also the oxidation-coupled increase in the pre-edge magnitude (insets in Fig. 2a and c), pointing towards analogous structural changes. The extended X-ray absorption fine-structure (EXAFS) provides more specific insight (Fig. 2b and d). The similarity between the spectra of the biological and synthetic catalyst suggests prevalence of similar structural motifs. In line with EXAFS simulations (ref. 32 for PSII; ESI,† Fig. S4 and Table S1 for the Mn oxides), the first peak is assigned to oxygen atoms in the first Mn coordination sphere. For increasingly positive potentials, its amplitude increases because of increasingly homogeneous distribution of Mn–O distances. This is explainable by oxidation of Mn^{III} ions, which typically exhibit Jahn–Teller elongation resulting in a broad inhomogeneous distance distribution and thus low peak-1 amplitude.[11–14,32] The second peak corresponds to short metal–metal distances (<2.9 Å) of two manganese ions connected by two bridging oxygen atoms (di-μ-oxo bridging, edge-sharing of MnO_6 octahedra). The increase of the peak-2 amplitude signifies an increase in the number of these short Mn–Mn distances either by formation of additional μ-oxo bridges or by deprotonation of existing (longer) μ-hydroxo bridges. The third peak, well visible in the oxide spectra, corresponds to distances around 3.4 Å explainable by mono-μ-oxo bridging between the metal ions.[12,39] In the Fourier-transformed EXAFS spectra of the inactive Mn oxide (Fig. 2f), peak 6 indicates the presence of co-linearly arranged Mn ions (rows of three edge-sharing MnO_6 octahedra) and peaks 4–5 relate to the diagonal distances expected for a layered MnO_2; the coordination number of the 2.88 Å Mn–Mn vectors is close to 5 and thus close to the value of 6 predicted for an infinitely extended MnO_2 layer (ESI,† Table S1). In the catalytically active and 'defect-rich' MnCat, however, it is less clear to what extent the layer picture is appropriate; we cannot exclude formation of tunnel-like motifs as found, *e.g.*, in todorokites.[6]

Within the overall similar spectral shape of the biological Mn_4CaO_5 and the inorganic oxide catalysts, there are also differences, mainly due to a clearly higher number of interconnected Mn ions in the inorganic oxides. The number of di-μ-oxo connected Mn ions is larger in the synthetic oxides resulting in increased amplitudes of peak-II and peak-III. In the more extended structure of the synthetic oxides, most of the bridging oxygen atoms connect three Mn ions (μ_3-oxo bridge) as opposed to the higher percentage of μ_2-O bridging in the Mn_4CaO_5 cluster of PSII (herein the *i* in μ_i-O does not include the comparatively weak bonding to the Ca ion). Since the Mn–O and Mn–Mn distances are typically longer in the case of μ_3-oxo bridging, peak-1 (Mn–O) and peak-2 (Mn–(μ_2-O)–Mn) are at slightly shorter distances in the biological catalyst. Regardless of these subtle differences in the static structure, the changes in the spectra of the biological catalyst and the water-oxidizing oxide (MnCat) are surprisingly similar and suggest similar structural rearrangements.

Comparing catalytically active and inactive Mn oxides

To address the requirements for catalytic activity in the synthetic Mn oxides, we investigated a second Mn oxide, electrodeposited at constant potential, which is able to undergo extensive Mn oxidation-state changes but exhibits negligible activity towards water oxidation (ESI,† Fig. S2).[13] Using UV-vis absorption to track Mn oxidation, we detect qualitatively similar changes in the catalytically active and inactive oxide (ESI,† Fig. S8). For quantitative analysis of the relation between absolute Mn oxidation states and applied electrochemical potential, we employed the X-ray absorption experiment, which reveals informative differences:

(1) In the inactive oxide, high potentials result in an all-Mn^{IV} state of the oxide, whereas in the active oxides we surprisingly find stable Mn^{III} ions that are not oxidized, even at highest investigated potentials, as evident from the Mn oxidation state estimated from XANES data (Fig. 3).

(2) The inactive oxides are more ordered as evidenced by higher amplitudes of peak-2 and peak-6 of the Fourier-transformed (FT) EXAFS spectra, where the latter FT peak is attributed to a sequence of three collinearly arranged di-μ-oxo bridged Mn ions detectable

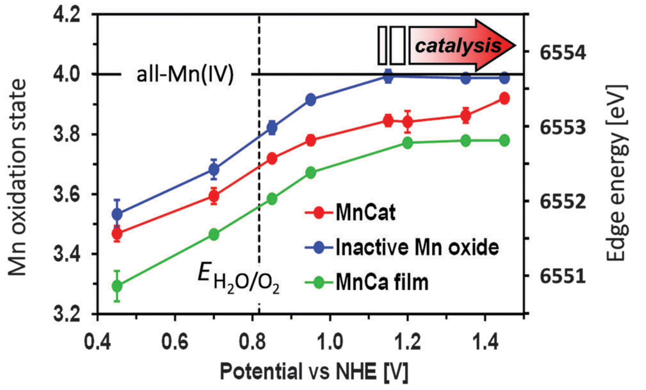

Fig. 3 Mean Mn oxidation state (left *y*-axis) at different electrode potentials estimated from the X-ray edge-position energy (right *y*-axis) for the MnCat, the catalytically inactive Mn oxide, and the catalytically active MnCa film. A calibration curve relating Mn oxidation state and Mn edge-energy positions is shown in the ESI,† Fig. S3. Error bars represent standard errors calculated from 3–12 measurements. Vertical dotted line indicates the equilibrium potential for water oxidation at pH 7. XANES spectra of the MnCa oxide are shown in ESI,† Fig. S7a.

only in relatively well ordered Mn oxides.[13] These relatively minor 'static' differences between MnCat and the inactive Mn oxide were already reported before in XAS studies on dry films[13] or films measured after removal of the electrode potential, under open-circuit conditions.[15] Here, we investigate these materials, for the first time, under electrochemical operation conditions and show that the basic structural difference is maintained for application of electrode potentials ranging from the clearly sub-catalytic to the catalytic regime (0.45 V to 1.45 V). However, the two oxides differ distinctly regarding structural changes in their response to increasing electrochemical potentials. The magnitude of the second Fourier peak (peak-2), assignable to di-μ-oxo bridging between Mn ions, is increasing (for increasingly positive potentials) in the active Mn oxide, but remains largely constant in the inactive oxide. This increase may be due to either deprotonation of existing μ-hydroxo bridges, or to formation of new μ-oxo bonds. The former option is predicted to result in increased damping of the EXAFS oscillation (increase in the EXAFS Debye–Waller parameter, σ) and is disfavored by the analysis shown in ESI,† Fig. S6. Similarly, peak-3 changes in the active oxide, but not so in the inactive oxide (compare Fig. 2d and f). We conclude that in the catalytically active oxide, the accumulation of oxidizing equivalents is accompanied by structural changes involving modification of the metal–metal bridging type, as also observed in the biological catalysts (Fig. 2b). In contrast, comparatively minor bridging-type changes are detectable in the inactive Mn oxide.

Trapped Mn^{III} ions in catalytically active Mn oxides

Comparison of the potential-dependence of oxidation states extends previous insight in the role of Mn^{III} ions.[12,13,40–45] Fig. 3 shows that for increasingly positive electrode potentials, the Mn oxidation state levels off at about 4.0 for the inactive oxides but at lower values for the catalytically active oxides. An oxidation state of 4.0 and the high amplitudes of peak-2 and peak-6 in the Fourier-transformed EXAFS spectra of the inactive Mn oxide (Fig. 2f) indicates formation of comparatively well ordered Mn^{IV} oxide structure, similar to the one shown in Fig. 1c, but containing also some corner-sharing MnO_6 octahedra (peak-3) as present in tunnel-forming $Mn^{IV}O_2$ modifications. In such a structure the majority of the manganese ions are embedded in an extended oxide structure, coordinatively mostly saturated by six μ_3-oxo ligands and thus likely unreactive. Therefore, we believe that the rigidness related to the all-Mn^{IV} structure found in the inactive oxide at catalytic potentials explains its lacking water oxidation activity. Suitable sites for substrate–water binding are unavailable and the oxide cannot undergo the structural and oxidation-state changes needed to facilitate the 4-electron–4-proton water-oxidation chemistry.

At a potential of about 1.25 V, we detect the onset of sizeable catalytic current (ESI,† Fig. S2); at this potential about 15% of Mn^{III} ions are still present in the structure of the catalytically active Mn oxides (20% in the MnCa oxide). Likely these Mn^{III} ions are stabilized by a metal–oxo environment created by (electro)-synthesis protocols which involve oxidative and reductive phases (alternating oxidizing-reducing potentials;[13] transient reduction by low-temperature annealing[30]). Seemingly, the 'trapped' Mn^{III} ions are characterized by a local increase of their Mn^{III}/Mn^{IV} midpoint potential. Clearly more positive electrochemical potentials—beyond the herein investigated potential range—are required for (stable) oxidation of the 'trapped' Mn^{III} ions, as compared to the potential needed for complete Mn^{III} oxidation in the catalytically inactive oxide material. We propose that the trapped Mn^{III} ions allow for formation of specific local clusters which are not present in the inactive $Mn^{IV}O_2$ oxide (as indicated by the EXAFS data) and likely constitute the active sites of water oxidation catalysis; even at highly oxidizing, catalytic potential, they can undergo changes in oxidation and protonation state, coordination number and bridging type. It has been proposed that the presence of out-of-layer corner-sharing Mn^{III} centers is decisive for catalytic activity of Mn oxides.[45] Being in line with this hypothesis, our results extend it further by showing that the stabilization of a fraction of Mn^{III} centers at electrochemical potentials relevant for O_2 evolution is crucial for catalytic performance. However our results clearly contradict a recent hypothesis that Mn^{III} oxidation to the all-Mn^{IV} state favors catalytic performance when it occurs already at comparably low electrode potentials (observed for noble metals in the oxide structure).[46]

Role of calcium ions

In the biological Mn_4CaO_5 catalyst, the Ca^{2+} ion is essential for optimal water-oxidation activity. To address the role of Ca^{2+}, we investigated mixed MnCa oxides formed by electrodeposition and subsequent annealing at 210 °C with catalytic activity similar to the Mn-only oxides discussed above.[30] The mixed MnCa oxides exhibit an atomic structure with a low degree of order and similar structural motifs as found in the Mn-only oxides. The Ca ion is connected *via* bridging oxygens to Mn ions, possibly forming a $Mn_3Ca(\mu\text{-}O)_4$ cubane structure,[12,30] in close analogy to the metal–oxo core of the biological catalyst. Comparison of XANES and EXAFS of the Mn-only and the MnCa oxide reveals similar oxidation state and structural changes (Fig. 2c and d and ESI,† Fig. S7). Interestingly, the incorporation of Ca results in an overall slightly lower mean Mn oxidation state (Fig. 3). The tuning of Mn redox potentials by coordination of Ca ions to bridging oxygen atoms has been reported also for structurally closely related Mn(Ca) complexes.[47] We conclude that the Ca ions prevent the formation of highly ordered oxide structures and further stabilize the Mn^{III} ions against (irreversible) oxidation at higher overpotentials.

Sequence and timescale of events

In the biological catalyst, 3 flashes of visible light induce 3 oxidation steps, which proceed within tens to hundreds of microseconds[48,49] and result in accumulation of 3 oxidizing equivalents by means of 3 $Mn^{III/IV}$ oxidation steps (Fig. 1b).[32,37,50] The removal of the fourth electron from the Mn_4Ca complex in PSII and the coupled O–O bond formation step proceed within about 2 ms.[48,49] In the synthetic oxides, we addressed the rate of Mn oxidation by means of new *in situ* X-ray and UV-vis experiments which facilitate time-resolved tracking of Mn oxidation-state changes.

In the experiment of Fig. 4a, the transition from open-circuit conditions (OCP) to application of a positive potential was investigated by detecting UV-vis absorption changes, which

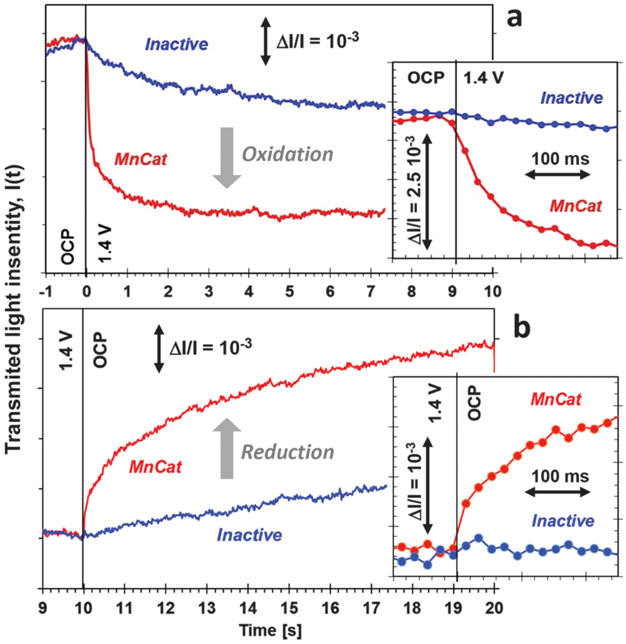

Fig. 4 Time-resolved UV-vis detection of oxidation state changes for the catalytically active Mn oxide (MnCat, red) and the inactive oxide (blue). The transmitted light intensity (blue light, around 470 nm) decreases/increases for oxidation/reduction of the catalyst film. (a) Transients for transition from open-circuit conditions (OCP) to application of an electric potential (1.4 V *vs.* NHE, pH 7). The time courses of the currents facilitating catalysts oxidation are shown in ESI,† Fig. S10. (b) Transients for a transition from applied electrode potential to OCP conditions. Under OCP conditions, there is no external current flow; the observed catalyst reduction likely results from Mn reduction coupled to water oxidation and O_2 formation.[28] The concomitant changes in the open-circuit potential are shown in ESI,† Fig. S10. The insets show the fast phases of the transients using an expanded time scale. We note that in the data of Fig. 4a, the Ohmic losses of the current flow through substrate electrode (ITO) and electrolyte (100 mM phosphate buffer) result in a slowing down of the transients (specifically for the active oxide), whereas under OCP conditions, the 'internal currents' are not affected by the external Ohmic losses. The transmitted-light signal detected before transition between OCP and applied potential (or *vice versa*) is denoted as I_0; the length of the double-arrowed bars indicates a relative change ($\Delta I/I_0$) in the intensity of the transmitted light by 10^{-3} (in all panels).

reflect oxidation state changes of the Mn ions in the catalyst film (compare Fig. 3 and ESI,† Fig. S8). We find that in the catalytically active film the oxidation state changes are clearly faster (by a factor of 10 or more) than in the inactive oxide. Fig. 4b shows the UV-vis transients for the transition from catalytic potential to OCP conditions, where the electrode is electrically insulated so that (external) electrical currents cannot flow. In the active oxide, a fast reduction is observed, which is most likely assignable to catalyst reduction coupled to water oxidation. This observation illustrates the employment of 'stored' (accumulated) oxidation equivalents for water oxidation which continues, for a short time period, even after removal of the external electric voltage, as previously shown for a hydrated Co-based catalyst film.[28] We estimate that in the inactive oxide after the transition to OCP conditions, the initial rate of catalyst reduction is roughly by two orders of magnitude slower than in the MnCat (see ESI,† Fig. S9).

Sudden changes in the potential of the catalyst electrode were combined with time-resolved detection of the X-ray fluorescence excited at 6553.3 eV, as shown in Fig. 5a (regarding choice of the excitation energy, see ESI,† Fig. S11). By means of this experiment, we also find that Mn redox-state changes are several-fold faster in the catalytically active than in the inactive oxide. The X-ray transients extend the insight obtained by the UV-vis data by providing evidence that the millisecond oxidation/reduction reactions detected in the UV-vis experiment can be assigned to Mn-centered redox chemistry (*versus* ligand centered chemistry, *e.g.* OH radical or peroxide formation). In the MnCat, about 35% of the Mn ions are changing their oxidation state within 10 s (see ESI,† Fig. S11c, left *y*-axis), which is in line with the steady-state data of Fig. 3. In the inactive oxide only about 20% of the Mn ions are oxidized/reduced in the voltage jump experiment because the oxidation state changes are not completed within 10 s.

Quantitative evaluation of the X-ray and UV-vis data transients is hampered by their pronouncedly non-exponential character. Moreover, the time-resolved potential-jump data cannot be easily corrected for the influence of the Ohmic resistance of electrolyte and substrate electrode. For detailed quantitative information on the sequence and time scale of events, electrochemical impedance spectroscopy (EIS) was employed resulting in highly different spectra for active and inactive catalysts (Fig. 5b–d and ESI,† Fig. S12–S14). The EIS data were simulated according to an equivalent circuit (inset-1 in Fig. 5b)[51,52] which included resistance (R_{OX}) and capacitance (C_{OX}) both related to the Mn oxidation state changes as well as a 'catalytic resistance' (R_{CAT}). This is the least complex equivalent-circuit model that provides an adequate simulation quality. Our time-resolved UV-vis and XAS data motivate and support the choice of this model, specifically regarding its relation to Mn oxidation state changes and catalysis. (The complete equivalent-circle model used in simulation of the impedance spectra also included an Ohmic resistance and a double-layer capacitance describing processes in the microsecond time domain which are, most likely, unrelated to the water oxidation chemistry of the hydrated oxides, see ESI,† Fig. S14.) We find that the catalytic resistance is by two orders of magnitude smaller in the catalytically active oxide (MnCat) than in the inactive oxide (ESI,† Fig. S14), confirming a pronounced difference in catalytic activity. In the catalytically active oxide, R_{CAT} is by about one order of magnitude higher than R_{OX} indicating that the oxidation-state changes are faster than the rate-determining chemical steps in O_2 formation ($k_{OX} > k_{CAT}$). In conjunction with the UV-vis and XAS results, this finding implies that the transiently stable accumulation of oxidizing equivalents in metal-centered oxidation steps ($Mn^{III\rightarrow IV}$ oxidation *vs.* O–ligand oxidation) precedes the water-oxidation/metal-reduction step, as has been suggested for a Co-based water oxidation catalyst[28,53–55] and as is the case in the biological catalyst.

Two reciprocal rate constants (time constants) were calculated from the EIS parameters: τ_{OX} (=$R_{OX}C_{OX}$) for the oxidation-state changes and τ_{CAT} (=$R_{CAT}C_{OX}$) for the catalytic reaction itself. Although their precise meaning is model dependent, these numbers provide access to the timescale of the events taking place in the catalyst material. The values of τ_{CAT} at 1.4 V *vs.* NHE

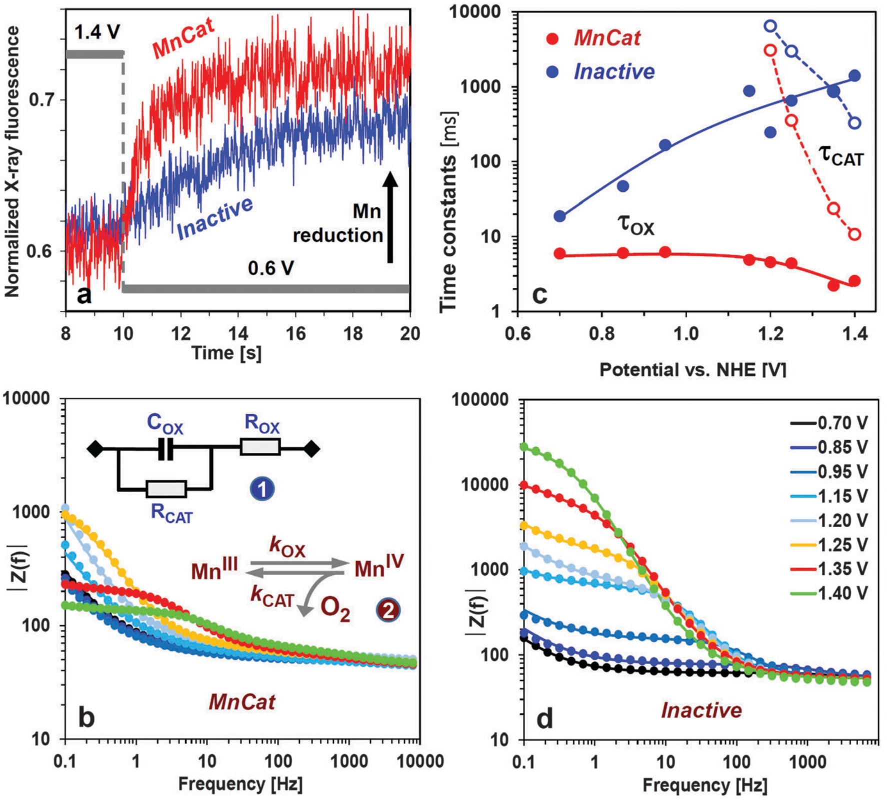

Fig. 5 Reaction kinetics investigated by time-resolved X-ray experiments (a) and EIS (b–d). (a) Mn oxidation-state changes of catalytically active Mn oxide (red) and inactive oxide (blue) induced by stepping the electrode potential from 1.4 V to 0.6 V and tracked by recording the $K_{\alpha/\beta}$ X-ray fluorescence intensity for excitation at 6553.3 eV (see also ESI,† Fig. S11). (b and d) Impedance spectra of the catalytically active oxide (MnCat, in (b)) and inactive oxide (in (d)), for sinusoidal modulation of the electric potential with an amplitude of 10 mV and frequencies ranging from 0.1 to 10 000 Hz (color coding of the mean potential in (d)). The solid lines were obtained by simulation (curve-fitting) involving equivalent circuit shown in inset-1 in (b). Simulation parameters and the corresponding phase spectrum are shown in ESI,† Figs. S12–S14. (c) Time constants calculated from parameters obtained by EIS simulations ($\tau_{OX} = R_{OX}C_{OX}$; $\tau_{CAT} = R_{CAT}C_{OX}$). For the (approximate) model of inset-2 (in (b)), τ_{OX} and τ_{CAT} are equal to $(k_{OX})^{-1}$ and $(k_{CAT})^{-1}$ (see ESI†).

is −2 orders of magnitude greater (slower) in the inactive oxide than in the active oxide (MnCat), in line with the estimates of the initial rate of Mn reduction coupled to O_2-formation derived from the time-resolved UV-vis data of Fig. 4b.

It comes as a surprise that the events in the catalytically active Mn oxide approach values of 10 ms ($k_{CAT}{}^{-1}$) and 2 ms ($k_{OX}{}^{-1}$) (at overpotentials of about 0.5 V) which are not much slower than in the biological catalyst (Fig. 5c). The discrepancy between these numbers and the overall more sluggish kinetics of catalytically active Mn(Ca) oxides (TOF per Mn ion and evolved O_2 of about 0.01 s^{-1} [13]) suggests that the number of catalytically active sites is small in comparison to the total number of Mn ions.

Discussion

We find that in both the protein-bound biological catalyst and the here investigated water-oxidizing Mn(Ca) oxides, oxidizing equivalents are accumulated in $Mn^{III} \rightarrow Mn^{IV}$ transitions, coupled to changes in the μ-oxo bridging. In the biological catalyst and likely also in the synthetic oxides, the accumulation of oxidizing equivalents by Mn oxidation precedes the onset of a multi-electron reaction resulting in O^{2-} oxidation and O–O bond formation.[56] The metal–oxo catalyst is characterized by Mn ions strongly coupled by di-μ-oxo bridging, but catalytic activity requires deviations from the structural motifs found in well-ordered MnO_2 layers. Structural motifs close to metal–oxo cubanes are found in the biological catalyst and likely are present in the synthetic oxides as well. The radical-coupling motif proposed to facilitate the efficient O–O bond formation chemistry in PSII requires a specific co-linear Mn–O···O–Mn arrangement that is not possible in layered MnO_2 structures (see ref. 57; also alternative mechanistic proposals are discussed[1,56,58]). Yet this specific atom arrangement could well be present in the disordered water-oxidizing manganese oxides (see Fig. 1d). We are still far away from knowing the active-site structure and mechanism of O–O bond formation in the water-oxidizing Mn oxides. However, it clearly is conceivable that the basic mode of water oxidation at the protein-bound MnCa–oxo cluster of PSII and in water-oxidizing Mn oxides is similar.

The classical picture of electrochemical water oxidation at electrode surfaces comprises four steps of pairwise electron-proton removal from water and peroxide species coordinated at a single metal site of an otherwise static oxide surface.[56] Influential computational studies on heterogeneous water oxidation root in this paradigm.[59–61] The picture of a dynamic catalyst material outlined above suggests that the mechanism of heterogeneous water oxidation in the herein investigated amorphous oxides could differ significantly from the classical prototype mechanism. Our investigation of the dynamic response of water-oxidizing Mn(Ca) oxides to increasingly positive electrochemical potentials suggests: (i) fast metal-ion oxidation and charge-compensating deprotonation in a bulk material which consists of oxide fragments and interfacing water layers, (ii) accumulation of (several) oxidizing equivalents by metal ion oxidation before onset of the O–O bond formation chemistry, and (iii) structural modification (variation of metal–metal bridging) of the oxide fragments in the bulk volume. These features (i–iii) imply that not a single metal center, but rather a functional unit of molecular dimensions, which can undergo oxidation-state as well as structural changes, is involved in catalysis of water oxidation. Thus mechanistic principles frequently discussed in the context of water oxidation by the protein-bound Mn_4Ca complex of PSII or by molecular transition-metal complexes are more suitable to describe the function of metal-oxide catalysts.[56] Therefore we believe that understanding of heterogeneous water-oxidation catalysis by the amorphous Mn(Ca) oxides may be best approached involving (also) a 'molecular picture' which includes mechanistic concepts developed for water oxidation by the protein-bound Mn_4Ca complex and homogeneous catalysts.

The following working hypothesis could explain why oxidation state changes in inactive Mn oxide are dramatically slower than in the MnCat: in both oxides, massive Mn oxidation occurs in the bulk material which requires a charge compensating process. In the catalytically active MnCat, this is the comparably fast deprotonation of bridging or terminal water ligands coupled to local structural changes. In the inactive oxide, similar deprotonation-coupled structural changes cannot take place because this oxide is, at all potentials, too close to a perfect $Mn(\mu\text{-}O)_2$ structure; thus the charge compensation associated with Mn oxidation involves comparably slow ion exchange throughout the bulk oxide, specifically release of potassium cations and/or uptake of phosphate anions.

Regarding development of Mn-based catalysts for water oxidation, our results suggest importance of the following aspects:

(1) Redox-active materials, which can accumulate oxidizing equivalents, are not *per se* good water oxidation catalysts. For sizable catalytic activity, specific active-site structures likely are decisive. In Mn oxides, it seems essential that at catalytic potentials, Mn^{III} ions are present along with Mn^{IV} ions. Since catalytic potentials exceed significantly the typical potential for oxidation of Mn^{III} ions, they need to be stabilized in specific structures with locally shifted midpoint potential. The presence of Ca ions may support stabilization of these structural motifs. However, calcium is not an essential requirement for water oxidation by Mn oxides. In future catalyst generations, also other ions than calcium may promote structural flexibility and active-site formation.

(2) Non-crystalline materials with dynamic (flexible) structures at catalytic electrochemical potentials favor catalysis as they allow for both oxidation state and structural changes during catalysis. Such dynamic structures may exist not only in completely amorphous oxides, but also in thin surface layers of (some) crystalline Mn oxides. Amorphization activation, as reported for Mn-based and Co-based catalysts,[20,27] and even reversible surface amorphization[62,63] could play a role in the design of future catalyst generations. However, not only the general ability of the oxide material to undergo redox-state changes appears to be a prerequisite for catalytic activity. It likely also is of importance whether the redox transitions are slow or fast. This conjecture roots in the time-resolved UV-vis and XAS data of Fig. 4 and 5, which represent a novel type of experiments for direct monitoring of redox-state changes of the metal ions in the time domain (and is confirmed by electrochemical impedance spectroscopy). We find that in the active Mn oxide, the redox-state changes are dramatically faster than in the inactive oxide (by one to two orders of magnitude), strongly suggesting that fast redox-state changes are essential for high catalytic activity.

Conclusions

In summary, we have characterized three exemplary Mn-based oxides, which all resemble amorphous minerals of the birnessite type. Upon exposure to a series of electrochemical potentials, we find Mn oxidation state and structural changes for the catalytically active oxides that are similar to those occurring in the Mn_4CaO_5 cluster of PSII in the reaction cycle of biological water oxidation. In the biological catalyst, it is well established that accumulation of oxidizing equivalents precedes a multi-electron step of O_2-formation involving several Mn ions; the same likely holds also for the synthetic Mn oxide catalysts.

It has been noted before that the ability to undergo oxidation-state changes is a crucial determinant of catalytic activity of water-oxidizing oxides.[24,26,28,46] We now identify two further, likely interrelated prerequisites for catalytic activity of amorphous Mn oxides: (i) the presence of Mn^{III} ions at catalytic potentials and thus avoidance of an inert all-Mn^{IV} oxide and (ii) fast rates of redox-state changes approaching the millisecond time domain.

In summary, rather than being 'biomimetic rocks',[64] the water-oxidizing Mn(Ca) oxides are dynamic materials characterized by fast chemical changes in their bulk volume. Their dynamic redox properties, including the rate (constants) of metal-centered oxidation state changes, are crucial determinants of catalytic activity. This is a new facet of water-oxidizing oxides that clearly deserves becoming a focal point of future investigation. We note in passing that the finding of fast redox dynamics of hydrated Mn oxides could also enrich the discussion of properties and functionality of manganese oxides in different contexts, *e.g.* biogenic manganese oxides, catalysis of various reactions, or metal ion sequestering (remediation).[6,9,65]

Acknowledgements

We thank the Deutsche Forschungsgemeinschaft (DFG) for financial support to the collaborative research center on Protonation Dynamics in Protein Function (SFB 1078, project A4/Dau) and the Berlin Cluster of Excellence on Unifying Concepts in Catalysis (UniCat, EXL 31411). We also acknowledge support by the Bundesministerium für Bildung und Forschung (BMBF, MEOKATS project, 03SF0433B). We thank the Helmholtz-Zentrum Berlin (HZB) for beamtime allocation at the beamlines KMC-3 and KMC-1 of the BESSY II synchrotron in Berlin-Adlershof; and we gratefully acknowledge technical support by Franz Schäfers, Marcel Mertin, and M. Gorgoi (all HZB/BESSY II, Berlin Adlershof). We thank Michael Haumann (Berlin) and Philipp Kurz (Freiburg) for stimulating discussion.

References

1 J. P. McEvoy and G. W. Brudvig, *Chem. Rev.*, 2006, **106**, 4455–4483.

2 J. Barber, *Chem. Soc. Rev.*, 2009, **38**, 185–196.

3 N. Cox, D. A. Pantazis, F. Neese and W. Lubitz, *Acc. Chem. Res.*, 2013, **46**, 1588–1596.

4 H. Dau, I. Zaharieva and M. Haumann, *Curr. Opin. Chem. Biol.*, 2012, **16**, 3–10.

5 M. Suga, F. Akita, K. Hirata, G. Ueno, H. Murakami, Y. Nakajima, T. Shimizu, K. Yamashita, M. Yamamoto, H. Ago and J.-R. Shen, *Nature*, 2015, **517**, 99–103.

6 J. E. Post, *Proc. Natl. Acad. Sci. U. S. A.*, 1999, **96**, 3447–3454.

7 K. Sauer and V. K. Yachandra, *Proc. Natl. Acad. Sci. U. S. A.*, 2002, **99**, 8631–8636.

8 M. J. Russell, J. F. Allen and E. J. Milner-White, in *Photosynthesis, Energy from the Sun: 14th International Congress on Photosynthesis*, ed. J. F. Allen, E. Gantt, J. H. Golbeck and B. Osmond, Springer, 2008, pp. 1187–1192.

9 T. G. Spiro, J. R. Bargar, G. Sposito and B. M. Tebo, *Acc. Chem. Res.*, 2010, **43**, 2–9.

10 J. E. Johnson, S. M. Webb, K. Thomas, S. Ono, J. L. Kirschvink and W. W. Fischer, *Proc. Natl. Acad. Sci. U. S. A.*, 2013, **110**, 11238–11243.

11 M. Wiechen, I. Zaharieva, H. Dau and P. Kurz, *Chem. Sci.*, 2012, **3**, 2330–2339.

12 I. Zaharieva, M. M. Najafpour, M. Wiechen, M. Haumann, P. Kurz and H. Dau, *Energy Environ. Sci.*, 2011, **4**, 2400–2408.

13 I. Zaharieva, P. Chernev, M. Risch, K. Klingan, M. Kohlhoff, A. Fischer and H. Dau, *Energy Environ. Sci.*, 2012, **5**, 7081–7089.

14 R. K. Hocking, R. Brimblecombe, L.-Y. Chang, A. Singh, M. H. Cheah, C. Glover, W. H. Casey and L. Spiccia, *Nat. Chem.*, 2011, **3**, 461–466.

15 G. Mattioli, I. Zaharieva, H. Dau and L. Guidoni, *J. Am. Chem. Soc.*, 2015, **137**, 10254–10267.

16 D. M. Robinson, Y. B. Go, M. Mui, G. Gardner, Z. Zhang, D. Mastrogiovanni, E. Garfunkel, J. Li, M. Greenblatt and G. C. Dismukes, *J. Am. Chem. Soc.*, 2013, **135**, 3494–3501.

17 F. Jiao and H. Frei, *Energy Environ. Sci.*, 2010, **3**, 1018–1027.

18 A. Ramírez, P. Hillebrand, D. Stellmach, M. M. May, P. Bogdanoff and S. Fiechter, *J. Phys. Chem. C*, 2014, **118**, 14073–14081.

19 Y. T. Meng, W. Q. Song, H. Huang, Z. Ren, S. Y. Chen and S. L. Suib, *J. Am. Chem. Soc.*, 2014, **136**, 11452–11464.

20 A. Indra, P. W. Menezes, I. Zaharieva, E. Baktash, J. Pfrommer, M. Schwarze, H. Dau and M. Driess, *Angew. Chem., Int. Ed.*, 2013, **52**, 13206–13210.

21 D. A. Pantazis, W. Ames, N. Cox, W. Lubitz and F. Neese, *Angew. Chem., Int. Ed.*, 2012, **51**, 9935–9940.

22 H. Dau and M. Haumann, *Biochim. Biophys. Acta*, 2007, **1767**, 472–483.

23 J. E. Post and D. R. Veblen, *Am. Mineral.*, 1990, **75**, 477–489.

24 M. Risch, K. Klingan, F. Ringleb, P. Chernev, I. Zaharieva, A. Fischer and H. Dau, *ChemSusChem*, 2012, **5**, 542–549.

25 Y. Surendranath, M. Dinca and D. G. Nocera, *J. Am. Chem. Soc.*, 2009, **131**, 2615–2620.

26 K. Klingan, F. Ringleb, I. Zaharieva, J. Heidkamp, P. Chernev, D. Gonzalez-Flores, M. Risch, A. Fischer and H. Dau, *ChemSusChem*, 2014, **7**, 1301–1310.

27 D. Gonzalez-Flores, I. Sanchez, I. Zaharieva, K. Klingan, J. Heidkamp, P. Chernev, P. W. Menezes, M. Driess, H. Dau and M. L. Montero, *Angew. Chem., Int. Ed.*, 2015, **54**, 2472–2476.

28 M. Risch, F. Ringleb, M. Kohlhoff, P. Bogdanoff, P. Chernev, I. Zaharieva and H. Dau, *Energy Environ. Sci.*, 2015, **8**, 661–674.

29 R. L. Doyle, I. J. Godwin, M. P. Brandon and M. E. G. Lyons, *Phys. Chem. Chem. Phys.*, 2013, **15**, 13737–13783.

30 D. Gonzalez-Flores, I. Zaharieva, J. Heidkamp, P. Chernev, E. M. Moreno, C. Pasquini, M. R. Mohammadi, A. Fischer and H. Dau, *ChemSusChem*, 2016, **9**, 379–387.

31 B. Kok, B. Forbush and M. McGloin, *Photochem. Photobiol.*, 1970, **11**, 457–475.

32 M. Haumann, C. Müller, P. Liebisch, L. Iuzzolino, J. Dittmer, M. Grabolle, T. Neisius, W. Meyer-Klaucke and H. Dau, *Biochemistry*, 2005, **44**, 1894–1908.

33 H. Dau, L. Iuzzolino and J. Dittmer, *Biochim. Biophys. Acta*, 2001, **1503**, 24–39.

34 Y. Gorlin, B. Lassalle-Kaiser, J. D. Benck, S. Gul, S. M. Webb, V. K. Yachandra, J. Yano and T. F. Jaramillo, *J. Am. Chem. Soc.*, 2013, **135**, 8525–8534.

35 L. Iuzzolino, J. Dittmer, W. Dörner, W. Meyer-Klaucke and H. Dau, *Biochemistry*, 1998, **37**, 17112–17119.

36 J. E. Penner-Hahn, R. M. Fronko, V. L. Pecoraro, C. F. Yocum, S. D. Betts and N. R. Bowlby, *J. Am. Chem. Soc.*, 1990, **112**, 2549–2557.

37 H. Dau, P. Liebisch and M. Haumann, *Anal. Bioanal. Chem.*, 2003, **376**, 562–583.

38 J. Messinger, J. H. Robblee, U. Bergmann, C. Fernandez, P. Glatzel, H. Visser, R. M. Cinco, K. L. McFarlane, E. Bellacchio, S. A. Pizarro, S. P. Cramer, K. Sauer, M. P. Klein and V. K. Yachandra, *J. Am. Chem. Soc.*, 2001, **123**, 7804–7820.

39 V. K. Yachandra, V. J. DeRose, M. J. Latimer, I. Mukerji, K. Sauer and M. P. Klein, *Science*, 1993, **260**, 675–679.

40 T. Takashima, K. Hashimoto and R. Nakamura, *J. Am. Chem. Soc.*, 2012, **134**, 1519–1527.

41 I. G. McKendry, S. K. Kondaveeti, S. L. Shumlas, D. R. Strongin and M. J. Zdilla, *Dalton Trans.*, 2015, **44**, 12981–12984.

42 X. Li, J. Liu, Y. Zhao, H. Zhang, F. Du, C. Lin, T. Zhao and Y. Sun, *ChemCatChem*, 2015, **7**, 1848–1856.

43 A. Indra, P. W. Menezes, F. Schuster and M. Driess, *J. Photochem. Photobiol., B*, 2015, **152**, 156–161.

44 C. H. Kuo, W. K. Li, L. Pahalagedara, A. M. El-Sawy, D. Kriz, N. Genz, C. Guild, T. Ressler, S. L. Suib and J. He, *Angew. Chem., Int. Ed.*, 2015, **54**, 2345–2350.

45 P. F. Smith, B. J. Deibert, S. Kaushik, G. Gardner, S. Hwang, H. Wang, J. F. Al-Sharab, E. Garfunkel, L. Fabris, J. Li and G. C. Dismukes, *ACS Catal.*, 2016, **6**, 2089–2099.

46 L. C. Seitz, T. J. P. Hersbach, D. Nordlund and T. F. Jaramillo, *J. Phys. Chem. Lett.*, 2015, **6**, 4178–4183.

47 E. Y. Tsui and T. Agapie, *Proc. Natl. Acad. Sci. U. S. A.*, 2013, **110**, 10084–10088.

48 W. Junge, M. Haumann, R. Ahlbrink, A. Mulkidjanian and J. Clausen, *Philos. Trans. R. Soc., B*, 2002, **357**, 1407–1418.

49 A. Klauss, M. Haumann and H. Dau, *J. Phys. Chem. B*, 2015, **119**, 2677–2689.

50 N. Cox, M. Retegan, F. Neese, D. A. Pantazis, A. Boussac and W. Lubitz, *Science*, 2014, **345**, 804–808.

51 B. Klahr, S. Gimenez, F. Fabregat-Santiago, J. Bisquert and T. W. Hamann, *J. Am. Chem. Soc.*, 2012, **134**, 16693–16700.

52 M. E. G. Lyons and M. P. Brandon, *J. Electroanal. Chem.*, 2009, **631**, 62–70.

53 M. W. Kanan and D. G. Nocera, *Science*, 2008, **321**, 1072–1075.

54 Y. Surendranath, M. W. Kanan and D. G. Nocera, *J. Am. Chem. Soc.*, 2010, **132**, 16501–16509.

55 J. B. Gerken, J. G. McAlpin, J. Y. C. Chen, M. L. Rigsby, W. H. Casey, R. D. Britt and S. S. Stahl, *J. Am. Chem. Soc.*, 2011, **133**, 14431–14442.

56 H. Dau, C. Limberg, T. Reier, M. Risch, S. Roggan and P. Strasser, *ChemCatChem*, 2010, **2**, 724–761.

57 P. E. M. Siegbahn, *Biochim. Biophys. Acta*, 2013, **1827**, 1003–1019.

58 N. Cox and J. Messinger, *Biochim. Biophys. Acta*, 2013, **1827**, 1020–1030.

59 J. Rossmeisl, Z. W. Qu, H. Zhu, G. J. Kroes and J. K. Norskov, *J. Electroanal. Chem.*, 2007, **607**, 83–89.

60 J. K. Norskov, T. Bligaard, J. Rossmeisl and C. H. Christensen, *Nat. Chem.*, 2009, **1**, 37–46.

61 I. C. Man, H. Y. Su, F. Calle-Vallejo, H. A. Hansen, J. I. Martinez, N. G. Inoglu, J. Kitchin, T. F. Jaramillo, J. K. Norskov and J. Rossmeisl, *ChemCatChem*, 2011, **3**, 1159–1165.

62 A. Bergmann, E. Martinez-Moreno, D. Teschner, P. Chernev, M. Gliech, J. F. de Araujo, T. Reier, H. Dau and P. Strasser, *Nat. Commun.*, 2015, **6**, 8625.

63 C. W. Tung, Y. Y. Hsu, Y. P. Shen, Y. X. Zheng, T. S. Chan, H. S. Sheu, Y. C. Cheng and H. M. Chen, *Nat. Commun.*, 2015, **6**, 8106.

64 M. Wiechen, H.-M. Berends and P. Kurz, *Dalton Trans.*, 2012, **41**, 21–31.

65 S. L. Suib, *Acc. Chem. Res.*, 2008, **41**, 479–487.